Available online at www.sciencedirect.com
SCIENCE DIRECT®
Journal of Computational Physics 215 (2006) 348–362
JOURNAL OF COMPUTATIONAL PHYSICS
www.elsevier.com/locate/jcp

Simulations of singularity dynamics in liquid crystal flows: A C^0 finite element approach

Ping Lin [a,*], Chun Liu [b]

[a] Department of Mathematics, The National University of Singapore, 2 Science Drive 2, Singapore 117543, Singapore
[b] Department of Mathematics, Pennsylvania State University, University Park, PA 18601, USA

Received 1 May 2005; received in revised form 14 September 2005; accepted 31 October 2005
Available online 15 December 2005

Abstract

In this paper, we present a C^0 finite element method for a 2D hydrodynamic liquid crystal model which is simpler than existing C^1 element methods and mixed element formulation. The energy law is formally justified and the energy decay is used as a validation tool for our numerical computation. A splitting method combined with only a few fixed point iteration for the penalty term of the director field is applied to reduce the size of the stiffness matrix and to keep the stiffness matrix time-independent. The latter avoids solving a linear system at every time step and largely reduces the computational time, especially when direct linear system solvers are used. Our approach is verified by comparing its computational results with those obtained by C^1 elements and by mixed formulation. Through numerical experiments of a few other splittings and explicit–implicit strategies, we recommend a fast and reliable algorithm for this model. A number of examples are computed to demonstrate the algorithm.

MSC: 65M60; 76A15

Keywords: Liquid crystal flow; Finite element approximation; Splitting method

1. Introduction

There are growing interests about the theory and computation of liquid crystals among physicists and mathematicians. Liquid crystal materials not only see many important industrial applications [5,8], they can also be considered to be simple examples of elastic complex fluids. The hydrodynamical and rheological properties of the materials reflect the competition between the kinetic and elastic energies, through the transport of the orientational order parameter. The motivation of this paper is to develop an effective and robust numerical tool to illustrate and investigate such competitions.

Liquid crystal materials do not show a single transition from solid to liquid, but rather a cascade of transitions involving new phases. Classical Oseen–Frank theory suggests that the nematic phase of liquid crystals

* Corresponding author. Tel.: +65 6874 2488; fax: +65 6779 5452.
E-mail addresses: matlinp@nus.edu.sg (P. Lin), liu@math.psu.edu (C. Liu).

0021-9991/$ - see front matter
doi:10.1016/j.jcp.2005.10.027

can be described by an orientational order parameter or a director field $\mathbf{d}$, which minimizes so called Oseen–Frank elastic energy functional. The energy dictates the tendency of the orientational director being aligned to each other. This macroscopic orientational order parameter can also be derived through the microscopic kinetic equation as the eigenvector of the second moment [8]. Mathematical analysis and computation for some special cases of Oseen–Frank model may be found in [1,3,4,8,10–13]. To describe liquid crystal flows we need not only the orientation, as represented by the director field $\mathbf{d}$, but also a macroscopic motion, represented by the velocity field $\mathbf{u}$. Ericksen and Leslie derive a hydrodynamic model for nematic liquid crystals. A nematic flow behaves like a regular liquid with molecules of similar size. However, it displays anisotropic properties due to the molecule alignment described by the local director field $\mathbf{d}$. In order to understand Ericksen–Leslie theory from the analysis point of view, Lin and Liu [14] proposed to consider a simplified model which retains most mathematical and physical significance of the original system and at the same time is possible for rigorous analysis. The model also emphasizes the special coupling between the director and the flow field. The model reads

$$\mathbf{u}_t + (\mathbf{u}\cdot\nabla)\mathbf{u} - \nu\nabla\cdot D(\mathbf{u}) + \nabla p + \lambda\nabla\cdot((\nabla\mathbf{d})^{\mathrm{T}}\nabla\mathbf{d}) = 0, \tag{1.1}$$

$$\nabla\cdot\mathbf{u} = 0, \tag{1.2}$$

$$\mathbf{d}_t + (\mathbf{u}\cdot\nabla)\mathbf{d} - \gamma(\Delta\mathbf{d} - \mathbf{f}(\mathbf{d})) = 0 \tag{1.3}$$

with initial and boundary conditions

$$\mathbf{u}|_{t=0} = \mathbf{u}_0, \quad \mathbf{d}|_{t=0} = \mathbf{d}_0, \quad \mathbf{u}|_{\partial\Omega} = \mathbf{u}_0|_{\partial\Omega} = \mathbf{g}_{\mathbf{u}}, \quad \mathbf{d}|_{\partial\Omega} = \mathbf{d}_0|_{\partial\Omega} = \mathbf{g}_{\mathbf{d}}.$$

Here, $\mathbf{u}$ represents the velocity of the liquid crystal flow, p the pressure, and $\mathbf{d}$ the orientation of the liquid crystal molecules, $\mathbf{u}, \mathbf{d}$: $\Omega\times\mathscr{R}^+ \to \mathscr{R}^n$, p: $\Omega\times\mathscr{R}^+ \to \mathscr{R}$ and $\Omega\subset\mathscr{R}^n$. In our computation, we will only consider $n = 2$, i.e. two-dimensional cases. Also, the strain rate $D(\mathbf{u}) = (1/2)(\nabla\mathbf{u} + (\nabla\mathbf{u})^{\mathrm{T}})$, the gradients of the director field take the standard notation as

$$(\nabla\mathbf{d})_{ij} = \mathbf{d}_{i,j} = \frac{\partial d_i}{\partial x_j}$$

and $\mathbf{f}(\mathbf{d}) = (1/\epsilon^2)(—\mathbf{d}|^2 - 1)\mathbf{d}$ is a penalty function used to approximate the constraint $|\mathbf{d}| = 1$ which is due to liquid crystal molecules being of similar size. $\mathbf{f}(\mathbf{d})$ is the gradient of the scalar valued function $F(\mathbf{d}) = (1/4\epsilon^2)(|\mathbf{d}|^2 - 1)^2$. The divergence operator of a matrix is defined as

$$(\nabla\cdot A)_i = a_{ij,j} = \sum_j \frac{\partial a_{ij}}{\partial x_j}.$$

The first equation in the system is the equation for the conservation of linear momentum (the force balance equation). It combines a usual equation describing the flow of an isotropic fluid and an extra nonlinear coupling term which is anisotropic. This extra term is the induced elastic stress from the elastic energy through the transport in the third equation. The second equation represents incompressibility of the liquid. The third equation is associated with conservation of the angular momentum. We want to point out the choice of the transport of the director, $\mathbf{d}_t + (\mathbf{u}\cdot\nabla)\mathbf{d}$, reflects the assumption that the molecule is small and only the transport of the center of the mass is taken into account.

It is expected that the flow velocity will influence the alignment of the molecule $\mathbf{d}$ by the transport of the vector. And the converse is also true, i.e. the change in alignment may induce velocity through the induced elastic stress. Even if the initial velocity is zero the evolution of the director field may induce a velocity (the phenomena having been coined as back-flow), and the velocity may in turn affect the evolution of the director field. Such special coupling makes the theoretical discussion, especially explicit analytical expression of the solutions, rather difficult for this complicated model (as will also be indicated in our later numerical examples). Numerical simulation of these phenomena is then interesting, or even necessary, to researchers in this area.

Some properties of the system of equations may be used to justify the correctness of simulation results. For instance, the director field satisfies the maximum principle, that is, its magnitude will not achieve a maximum

at any interior point of the space–time domain. Moreover, the system admits the following energy law (see [14]):

$$\frac{\mathrm{d}E}{\mathrm{d}t} = -\left(\nu\|D(\mathbf{u})\|^2_{L^2(\Omega)} + \lambda\gamma\|\Delta\mathbf{d} - \mathbf{f}(\mathbf{d})\|^2_{L^2(\Omega)}\right), \tag{1.4}$$

where

$$E = \frac{1}{2}\|\mathbf{u}\|^2_{L^2(\Omega)} + \frac{\lambda}{2}\|\nabla\mathbf{d}\|^2_{L^2(\Omega)} + \lambda\int_\Omega F(\mathbf{d}).$$

This indicates that the energy E should be decreasing in the time evolution. The formula of the energy E also reflects the competition of the kinetic and elastic energy. The constant λ is really the ratio between these two functionals. Moreover, the derivation of the energy law (1.4) also shows the coupling between the transport and the induced stress. The energy decreasing property may be used to justify the numerical method. This is in particular important when the singularities are involved, since the physical singularities we are after are those energetically admissible ones. There have been several previous attempts in this direction. Since in deriving this energy law the test function $\Delta\mathbf{d}$ is used (implying that the test function space should be in $\mathbf{H}^2$) a C^1 finite element method is adopted in [17] to solve the system (1.1)–(1.3) in order to keep the energy law in the numerical scheme. But the construction and implementation of C^1 element is complicated. In [18], they applied a mixed finite element method to the system to avoid the C^1 element. But the introduction of the new variable $W = \nabla\mathbf{d}$ increases the number of unknown variables and complication of implementation. Some other methods were used for this model, for example, a spectral method is used in [7] which is efficient for rectangular domains and periodic boundary conditions. In this paper, we will apply the Galerkin finite element method with C^0 elements directly to the system (1.1)–(1.3). The benefits of using such elements are obvious. The method can be implemented easily and many existing softwares and mesh generators may be incorporated to reduce complication. Numerical verification of the method and the energy decreasing law will be done through a number of examples. Some theoretical justification of the finite element formulation will be given in Section 2. In Sections 3 and 4, we introduce a splitting scheme combined with a fixed point iterative method to largely reduce the time of computing an evolution solution. We will use the method to simulate some interesting cases of the model with various parameters and domain geometries in Section 5. We hope that these computational results would motivate further theoretical study of the solution. Numerical experiments show that the method works very well for moderately small ϵ. Since we consider the two-dimensional case the energy is unbounded as ϵ approaches zero. When ϵ is extremely small we would not expect good performance of any numerical methods.

2. Weak formulation and finite element methods

Let Ω be a bounded domain of $\mathscr{R}^2$. We denote by Γ the boundary of Ω, and we suppose that Γ is sufficiently smooth (for example, Lipschitz-continuous). Define the spaces $\mathbf{H}^1(\Omega) = (H^1(\Omega))^2$, $\mathbf{H}^1_{\mathbf{g}} = \{\mathbf{u} \in \mathbf{H}^1(\Omega), \mathbf{u} = \mathbf{g} \text{ on } \Gamma\}$ and $\mathbf{L}^2(\Omega) = (L^2(\Omega))^2$.

A weak formulation of the system (1.1)–(1.3) reads:

Find $\mathbf{u} \in \mathbf{H}^1[0,\ T; \mathbf{H}^{-1}(\Omega)] \cap L^2[0,\ T; \mathbf{H}^1_{\mathbf{g_u}}(\Omega)]$, $p \in L^2[0,\ T; L^2(\Omega)/\mathscr{R}]$ and $\mathbf{d} \in \mathbf{H}^1[0,\ T; \mathbf{H}^1_{\mathbf{g_d}}]$ such that

$$\int_\Omega \left(\mathbf{u}_t \cdot \mathbf{v} + (\mathbf{u}\cdot\nabla)\mathbf{u}\cdot\mathbf{v} + \nu\nabla\mathbf{u} : \nabla\mathbf{v} - p(\nabla\cdot\mathbf{v}) - \lambda(\nabla\mathbf{d})^{\mathrm{T}}\nabla\mathbf{d} : \nabla\mathbf{v}\right)\mathrm{d}\mathbf{x} = \mathbf{0} \quad \forall\mathbf{v} \in L^2[0,T;\mathbf{H}^1_0(\Omega)], \tag{2.1}$$

$$\int_\Omega (\nabla\cdot\mathbf{u})q\,\mathrm{d}\mathbf{x} = 0 \quad \forall p \in L^2[0,T;L^2(\Omega)/\mathscr{R}], \tag{2.2}$$

$$\int_\Omega (\mathbf{d}_t\cdot\mathbf{e} + (\mathbf{u}\cdot\nabla)\mathbf{d}\cdot\mathbf{e} + \gamma(\nabla\mathbf{d} : \nabla\mathbf{e} - \mathbf{f}(\mathbf{d})\cdot\mathbf{e}))\,\mathrm{d}\mathbf{x} = 0 \quad \forall\mathbf{e} \in L^2[0,T;\mathbf{H}^1_0(\Omega)], \tag{2.3}$$

where ":" represents an inner product of two matrices, i.e. $A : B = \sum_i\sum_j a_{ij}b_{ij}$.

We first formally derive the energy decreasing property of the formulation when $\mathbf{u}$ and $\mathbf{d}$ satisfy homogeneous boundary conditions. From [18] and (1.3) we have

$$\nabla\cdot((\nabla\mathbf{d})^{\mathrm{T}}\nabla\mathbf{d}) = (\nabla\mathbf{d})^{\mathrm{T}}\Delta\mathbf{d} + \nabla(|\nabla\mathbf{d}|^2)/2 = \frac{1}{\gamma}(\nabla\mathbf{d})^{\mathrm{T}}(\mathbf{d}_t + (\mathbf{u}\cdot\nabla)\mathbf{d} + \gamma\mathbf{f}(\mathbf{d})) + \nabla(|\nabla\mathbf{d}|^2)/2$$
$$= \frac{1}{\gamma}(\nabla\mathbf{d})^{\mathrm{T}}(\mathbf{d}_t + (\mathbf{u}\cdot\nabla)\mathbf{d}) + \nabla\Big(|\nabla\mathbf{d}|^2/2 + F(\mathbf{d})\Big).$$

So for $\mathbf{u}$ and $\mathbf{d}$ in above defined spaces we weakly have

$$-\int_\Omega((\nabla\mathbf{d})^{\mathrm{T}}\nabla\mathbf{d}) : \nabla\mathbf{v}\,\mathrm{d}\mathbf{x} = \frac{1}{\gamma}\int_\Omega(\nabla\mathbf{d})^{\mathrm{T}}(\mathbf{d}_t + (\mathbf{u}\cdot\nabla)\mathbf{d})\cdot\mathbf{v}\,\mathrm{d}\mathbf{x} - \int_\Omega(|\nabla\mathbf{d}|^2/2 + F(\mathbf{d}))(\nabla\cdot\mathbf{v})\,\mathrm{d}\mathbf{x} \tag{2.4}$$

for all $\mathbf{v}\in\mathbf{H}_0^1(\Omega)$. Note that

$$(\nabla\mathbf{d})^{\mathrm{T}}\mathbf{d}_t\cdot\mathbf{u} = (\mathbf{u}\cdot\nabla)\mathbf{d}\cdot\mathbf{d}_t,$$
$$(\nabla\mathbf{d})^{\mathrm{T}}(\mathbf{u}\cdot\nabla)\mathbf{d}\cdot\mathbf{u} = |(\mathbf{u}\cdot\nabla)\mathbf{d}|^2$$

and define a new pressure p

$$p := p + |\nabla\mathbf{d}|^2/2.$$

Now substituting (2.4) into the last term of (2.1), taking $\mathbf{v}=\mathbf{u}$ and $\mathbf{e}=(\lambda/\gamma)\mathbf{d}_t$ in (2.1) and (2.3), respectively, summing them up and using integral identities (where (2.2) is used)

$$\int_\Omega(\mathbf{u}\cdot\nabla)\mathbf{u}\cdot\mathbf{u}\,\mathrm{d}\mathbf{x} = \frac{1}{2}\int_\Omega\mathbf{u}\cdot\nabla|\mathbf{u}|^2 = 0, \quad \int_\Omega(\mathbf{u}\cdot\nabla)\mathbf{d}\cdot\mathbf{f}(\mathbf{d}) = \int_\Omega\mathbf{u}\cdot\nabla F(\mathbf{d}) = 0,$$

we have the following energy law:

$$\frac{\mathrm{d}}{\mathrm{d}t}\left(\frac{1}{2}\|\mathbf{u}\|_{L^2}^2 + \frac{\lambda}{2}\|\nabla\mathbf{d}\|_{L^2}^2 + \lambda\int_\Omega F(\mathbf{d})\right) = -\left(\nu\|\nabla\mathbf{u}\|_{L^2}^2 + \frac{\lambda}{\gamma}\|\mathbf{d}_t + (\mathbf{u}\cdot\nabla)\mathbf{d}\|_{L^2}^2\right). \tag{2.5}$$

This indicates that the energy decays with time. Our numerical simulations later using our proposed finite element method based on (2.1)–(2.3) show that the energy decay is achieved in the examples we investigated. The rigorous discrete energy law shall involves with changing the induced elastic stress into terms with $\mathbf{d}_t$. This will be more important when the larger sized molecules are considered, hence the director $\mathbf{d}$ will take more complicated transport in (1.3), which in turn changes the induced elastic stress. We plan to pursue this issue in our future work. Nevertheless, numerical results obtained by our method will be verified by those existing results by the C^1 finite element method where the energy law is ensured. This indirectly provides verification of the energy law of our method. Meanwhile, energy decreasing is clearly a validation tool in numerical simulations of various examples.

Solutions of the weak problem (2.1)–(2.3) are approximated using an explicit–implicit finite difference scheme in time and a finite element method in spatial terms. Let

$$\mathbf{H} = \mathbf{H}_0^1(\Omega)\times L^2(\Omega)/\mathscr{R}\times\mathbf{H}_0^1(\Omega)$$

and $\mathbf{H}_h = \mathbf{U}_h\times\mathscr{P}_h\times\mathbf{W}_h\subset\mathbf{H}$ be a finite dimensional subspace of $\mathbf{H}$ given by a finite element discretization of Ω. If $\Delta t>0$ represents a time step size and $(\mathbf{u}_h^n, p_h^n, \mathbf{d}_h^n)\in\mathbf{H}_h$ is an approximation of $\mathbf{u}(t^n)=\mathbf{u}(n\Delta t)$, $p(t^n)=p(n\Delta t)$ and $\mathbf{d}(t^n)=\mathbf{d}(n\Delta t)$, the approximation at time $t^{n+1}=(n+1)\Delta t$ is computed as the solution of $(\mathbf{u}_h^{n+1}, p_h^{n+1}, \mathbf{d}_h^{n+1})\in\mathbf{H}_h$ by the following typical explicit–implicit scheme ("explicit" to avoid solving a nonlinear system in each time step):

$$\int_\Omega\left(\frac{\mathbf{u}_h^{n+1}-\mathbf{u}_h^n}{\Delta t}\cdot\mathbf{v} + (\mathbf{u}_h^n\cdot\nabla)\mathbf{u}_h^{n+1}\cdot\mathbf{v} + \nu\nabla\mathbf{u}_h^{n+1} : \nabla\mathbf{v} - p_h^{n+1}(\nabla\cdot\mathbf{v}) - \lambda(\nabla\mathbf{d}_h^n)^{\mathrm{T}}\nabla\mathbf{d}_h^n : \nabla\mathbf{v}\right)\mathrm{d}\mathbf{x} = \mathbf{0}, \tag{2.6}$$

$$\int_\Omega(\nabla\cdot\mathbf{u}_h^{n+1})q\,\mathrm{d}\mathbf{x} = 0, \tag{2.7}$$

$$\int_\Omega\left(\frac{\mathbf{d}_h^{n+1}-\mathbf{d}_h^n}{\Delta t}\cdot\mathbf{e} + (\mathbf{u}_h^n\cdot\nabla)\mathbf{d}_h^{n+1}\cdot\mathbf{e} + \gamma\nabla\mathbf{d}_h^{n+1} : \nabla\mathbf{e} + \frac{\gamma}{\epsilon^2}\Big(|\mathbf{d}_h^n|^2-1\Big)\mathbf{d}_h^{n+1}\cdot\mathbf{e}\right)\mathrm{d}\mathbf{x} = 0 \tag{2.8}$$

for all $(\mathbf{v}, q, \mathbf{e})\in\mathbf{H}$. The explicit–implicit scheme can be seen as one fixed point iteration of a fully implicit scheme of (2.6)–(2.8). Numerical experiments in the later part of this section indicate that it is good enough.

Remark 2.1. The divergence free condition (2.7) can be treated by a sequential regularization formulation so that general C^0 polynomial elements can be used and that we do not need to worry beforehand whether or not our elements would pass the Babuska–Brezzi test although it may be automatically satisfied via the formulation [15,16]. For this model it turns out that the penalty formulation (a simplest sequential regularization formulation and cf. [9,2]) has already worked well. That is, we replace (2.7) by the following:

$$\int_\Omega (\nabla \cdot \mathbf{u}_h^{n+1} + \delta p_h^{n+1}) q \, d\mathbf{x} = 0. \tag{2.9}$$

We choose $\delta = 10^{-6}$ in our computations. The divergence free condition is also numerically verified (in the sense of L^2 norm, i.e. $\sqrt{\frac{1}{|\Omega|}\int_\Omega |\nabla \cdot \mathbf{u}_h^{n+1}|^2 \, d\mathbf{x}}$) in our computations. For instance, in Example 2.2 below with a 16×16 grid the divergence free error is about 0.09 around $t = 0.25$ before the annihilation (existing singularities) and then the error is reduced quite a lot after the annihilation (no singularities). The error drops to about 0.0003 at $t = 0.75$ when the steady-state is reached.

Remark 2.2. If $\mathbf{u}$ and $\mathbf{d}$ satisfy non-homogeneous boundary conditions then $\mathbf{u}_h \in \mathbf{H}^1_{\mathbf{g_u}}$ and $\mathbf{d}_h \in \mathbf{H}^1_{\mathbf{g_d}}$ in the above finite element formulation.

Next we shall use the finite element method (2.6), (2.9) and (2.8) to compute a couple of 2D examples given in [17,18], where a C^1 element and a mixed finite element method are used. As in [17,18], we will set λ, ν and γ to be unity and $\Omega = (-1, 1) \times (-1, 1)$ with a uniform triangular mesh on a uniform square grid. We use the standard piecewise quadratic element for both $\mathbf{u}$ and $\mathbf{d}$ and then from (2.9) the pressure will be approximated by piecewise linear polynomials. So the Babuska–Brezzi condition is automatically satisfied. Whenever possible we will use a direct method (LU or Cholesky decomposition) to solve the resulting linear algebraic system since it may be more reliable than iterative methods for such complicated models. Our code is written with the help of the software Freefem++.

Example 2.1. We illustrate how singularities of opposite sign in the director field will move together and annihilate each other. We consider singularities of the form $\mathbf{d}(\mathbf{x}) = \tilde{\mathbf{d}}(\mathbf{x})/\sqrt{|\tilde{\mathbf{d}}(\mathbf{x})|^2 + \epsilon^2}$, where

$$\tilde{\mathbf{d}}(\mathbf{x}) = \omega(\mathbf{x}) A^-(\mathbf{x} + \mathbf{c}) + (1 - \omega(\mathbf{x})) A^+(\mathbf{x} - \mathbf{c}).$$

Here, $\omega(\mathbf{x}) = 1/(1 + \exp(5x_1))$, x_1 is the first component of $\mathbf{x}$, $A^\pm$ have diagonal $(\pm 1, 1)$ and the vector $\mathbf{c} = (1/2, 0)$. We take $\epsilon^2 = 0.25^2$ and $\Delta t = 0.001$. Fig. 1 plots the initial director field on a 5×5 grid (just for the purpose of comparison with the results in [18]) and the final director field at time $t = 1$. Fig. 2 shows the director and velocity fields near the annihilation of singularities (here 8×8 grid is used to better observe the velocity field). In our computation, the energy is clearly decreasing and $|\mathbf{d}| \leqslant 1$ which indicates both the energy law and

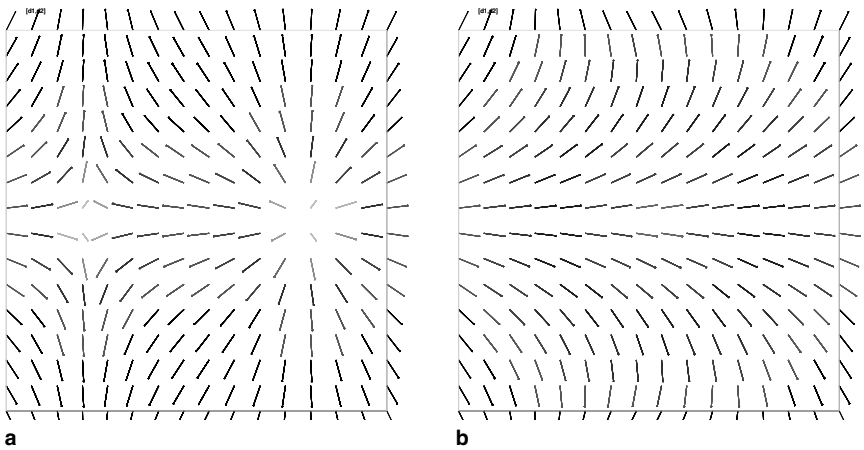

Fig. 1. Director fields $\mathbf{d}$ in a square domain: (a) $t = 0$; (b) $t = 1$.

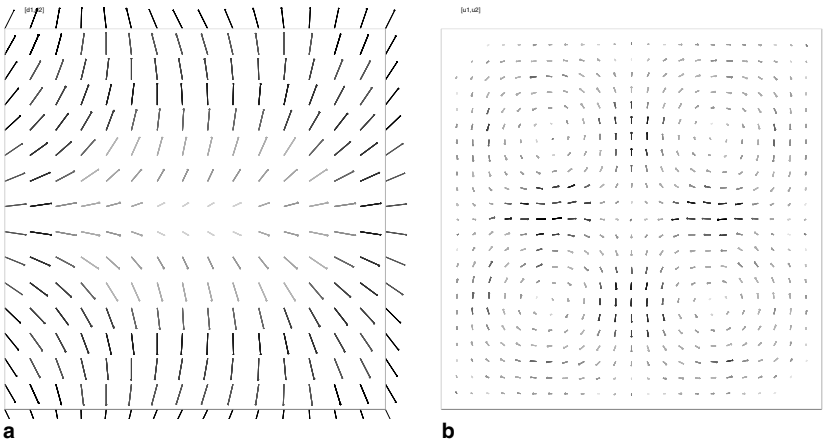

Fig. 2. Director and velocity fields near the annihilation time $t = 0.4$: (a) director field $\mathbf{d}$; (b) velocity $\mathbf{u}$.

the maximum principle for the director variable $\mathbf{d}$ are not violated in our algorithm. Also computational results coincide with those in [18] for the same example.

Example 2.2. We consider an example given in [17]. The initial director field $\mathbf{d}(\mathbf{x}) = \tilde{\mathbf{d}}(\mathbf{x})/\sqrt{|\tilde{\mathbf{d}}(\mathbf{x})|^2 + \epsilon^2}$, where

$$\tilde{\mathbf{d}}(\mathbf{x}) = (x_1^2 + x_2^2 - \alpha^2, 2\alpha x_2)$$

and $\alpha = 0.5$. This director field has singularities at $\mathbf{x} = (\pm\alpha, 0)$ with unit degrees of opposite signs. We use a uniform triangular mesh on a 16×16 grid and take $\epsilon^2 = 0.05^2$. Again we choose $\Delta t = 0.001$. We consider a zero initial velocity field first to see the annihilation of singularities. The evolution of this solution is shown in Fig. 3 where the initial and steady-state director fields (at $t = 0.75$) are shown. We also show the director and velocity fields near $t = 0.25$ in Fig. 4. To see more details of the velocity field we depict it using a 32×32 grid.

Then we choose the initial velocity field to be a rotating flow of the form $\mathbf{u} = (-\omega y, \omega x)$ with $\omega = 20$ (approximately three revolutions per unit time). Fig. 5 shows the initial velocity field and the director field at three different times, i.e. $t = 0.1$, $t = 0.2$ and the steady-state, say $t = 0.5$. All these results coincide with those in [17].

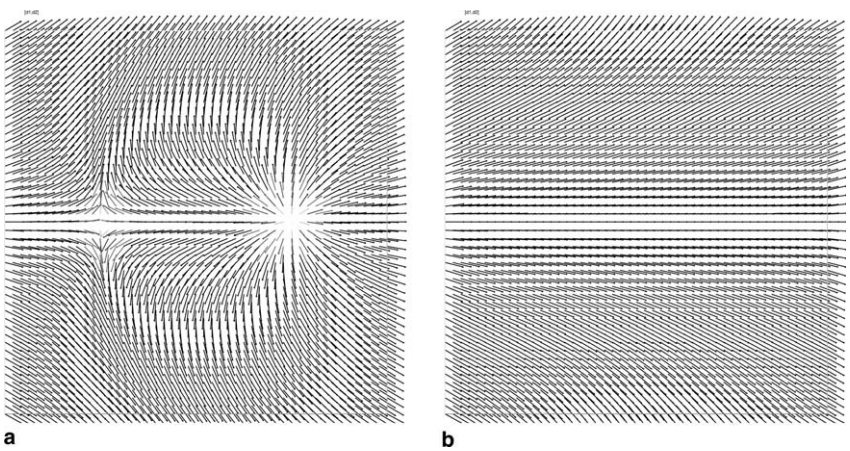

Fig. 3. Director fields with zero initial velocity: (a) $t = 0$; (b) $t = 0.75$.

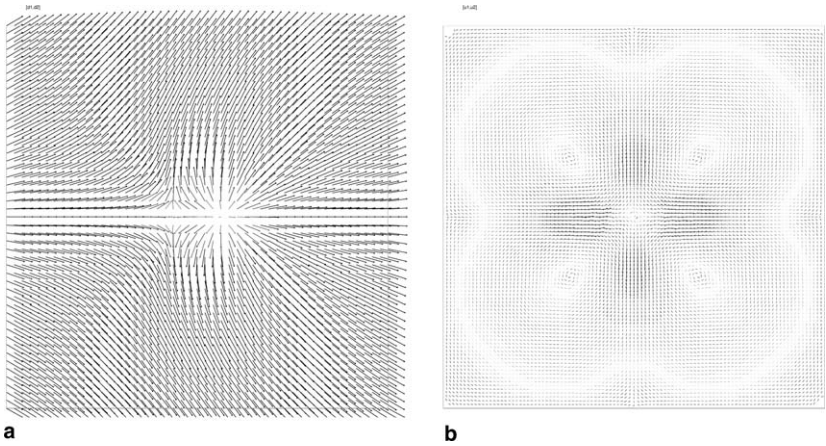

Fig. 4. Director and velocity fields near the annihilation time ($t = 0.25$) with zero initial velocity: (a) director field $\mathbf{d}$; (b) velocity field $\mathbf{u}$.

We remark finally that the energy at the singularity in the 2D model goes to infinity as ϵ goes to zero. So when ϵ is too small and/or when the number of singularities increases all numerical methods may suffer from the error caused at singularities. The evolution of singularity may be very sensitive to the algorithm and the mesh selected in the computation. Nevertheless, results for moderate values of ϵ should be pretty reliable and are usually enough to see the solution behavior.

3. Characteristic Galerkin method and splitting

In last section, we show that C^0 element works well for the liquid crystal flow computation. Since the C^0 element is much simpler than the C^1 element and/or the weak formulation is simpler than the mixed formulation used in [17,18], respectively. The computational time may be improved to some extent (typically half an hour CPU time on a Pentium 4 2.4 GHz PC with the $\mathscr{P}_2$ element on a 16×16 grid to evolve the solution through one unit of time). There is still a large room to further reduce the computational time if we observe in the above explicit–implicit scheme (2.6)–(2.8) the coupling of five equations and the common treatment of the convection term where the stiffness matrix of the finite element method changes with time, that is, we have to solve a pretty large linear system at every time step. We would like to use direct methods to solve the linear system which makes it even more time-consuming. Splitting methods may decompose the original problem into a number of subproblems associated with each sub-operator of the original problem. The subproblems will be solved separately and each subproblem is simpler to be dealt with and sometimes we can make the corresponding stiffness matrix of each subproblem independent of time so that when we use a direct method to solve it we only need to do LU or Choleski decomposition at the initial time and then only substitution is needed in obtaining the solution at following time steps.

Convection terms and time derivative terms

$$\int_\Omega (\mathbf{u}_t + (\mathbf{u} \cdot \nabla)\mathbf{u}) \cdot \mathbf{v} \, d\mathbf{x}$$

and

$$\int_\Omega (\mathbf{d}_t + (\mathbf{u} \cdot \nabla)\mathbf{d}) \cdot \mathbf{e} \, d\mathbf{x}$$

can be approximated by the characteristic Galerkin finite element method

$$\int_\Omega \frac{\mathbf{u}_h^{n+1} - \mathbf{u}_h^n(\mathbf{X}_\mathbf{u}^n)}{\Delta t} \cdot \mathbf{v} \, d\mathbf{x}$$

and

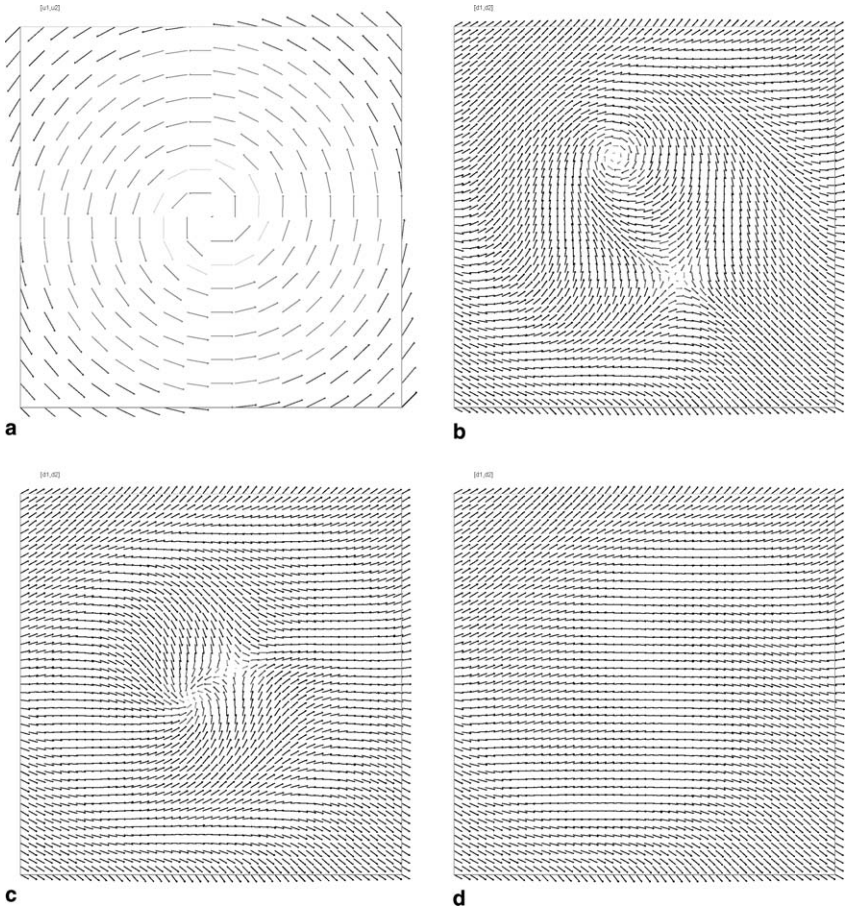

Fig. 5. Director fields $\mathbf{d}$ with an initial rotating flow field: (a) flow field at $t = 0$; (b) director field at $t = 0.1$; (c) director field at $t = 0.2$; (d) director field at $t = 0.5$.

$$\int_\Omega \frac{\mathbf{d}_h^{n+1} - \mathbf{d}_h^n(\mathbf{X}_\mathbf{d}^n)}{\Delta t} \cdot \mathbf{e}\, \mathrm{d}\mathbf{x},$$

respectively, where

$$\mathbf{X}_\mathbf{u}^n(\mathbf{x}) \approx \mathbf{x} + \mathbf{u}_h^n(\mathbf{x})\Delta t, \quad \mathbf{X}_\mathbf{d}^n(\mathbf{x}) \approx \mathbf{x} + \mathbf{u}_h^{n+1}(\mathbf{x})\Delta t.$$

It is shown that the characteristic Galerkin finite element is unconditionally stable up to quadrature errors in dealing with the convection term (see [6,19,20]). Moreover, the stiffness matrix associated with it would not depend on the time which will largely reduce the computational time in evolving the solution through a time interval. Nevertheless, due to the stiffness caused by the parameter ϵ^2 in the penalty term of Eq. (2.8) and accuracy requirement we would not choose our time step size Δt too large but smaller than ϵ^2 in order to have the stability. We can naturally (actually almost equivalently) split the scheme (2.6) and (2.7) as

$$\int_\Omega \left(\frac{\mathbf{u}_h^{n+1} - \mathbf{u}_h^n(\mathbf{X}_\mathbf{u}^n)}{\Delta t} \cdot \mathbf{v} + v\nabla \mathbf{u}_h^{n+1} : \nabla \mathbf{v} - p_h^{n+1}(\nabla \cdot \mathbf{v}) + \lambda(\nabla \mathbf{d}_h^n)^{\mathrm{T}} \nabla \mathbf{d}_h^n : \nabla \mathbf{v} \right) \mathrm{d}\mathbf{x} = \mathbf{0}, \tag{3.1}$$

$$\int_\Omega (\nabla \cdot \mathbf{u}_h^{n+1} + \delta p_h^{n+1}) q\, \mathrm{d}\mathbf{x} = 0 \tag{3.2}$$

and

$$\int_\Omega \left(\frac{\mathbf{d}_h^{n+1} - \mathbf{d}_h^n(\mathbf{X}_\mathbf{d}^n)}{\Delta t} \cdot \mathbf{e} + \gamma \nabla \mathbf{d}_h^{n+1} : \nabla \mathbf{e} + \frac{\gamma}{\epsilon^2} \left(|\mathbf{d}_h^n|^2 - 1 \right) \mathbf{d}_h^{n+1} \cdot \mathbf{e} \right) \mathrm{d}\mathbf{x} = 0 \tag{3.3}$$

for all $(\mathbf{v}, q, \mathbf{e}) \in \mathbf{H}$. In the velocity part of the scheme (3.1) and (3.2), we treat the convection term using characteristic finite element method and the other nonlinear term explicitly so that the stiffness matrix of the finite element method is independent of time t. In the second part of the scheme (3.3), we treat the convection term again by the characteristic finite element method. We would also like to treat the nonlinear term, i.e. the penalty term explicitly in order to make the resulting stiffness matrix independent of time t. It indeed work well for Example 2.1. However, when we apply it to Example 2.2 the annihilation of two defect points is a little bit slower than that of the non-splitting scheme (2.6)–(2.8) and the result in [17] although it provides correct steady-state solution. We thus suggest to use the above splitting scheme which treats the penalty term semi-implicitly as in (2.8). The resulting stiffness matrix of (3.3) remains time-dependent. Nevertheless, the computational time of the splitting scheme (3.1)–(3.3) is still much shorter than that of the scheme (2.6)–(2.8). The CPU time on a 16×16 grid is typically only 5 min to evolve the solution through one unit of time using the same computer mentioned at the beginning of the section. We run the scheme for the test examples given in the last section and obtain the same results. The energy decreasing property and $|\mathbf{d}| \leqslant 1$ (resulting from maximum principle) remain valid. These demonstrate that the splitting scheme with the help of characteristic Galerkin finite element is a faster and reliable scheme to compute the hydrodynamic liquid crystal model.

4. A fixed point iteration to achieve a time-independent stiffness matrix

As we mentioned in the previous section if we treat the penalty term in (3.3) fully explicitly the evolution of the defect points in Example 2.2 may be slower than those results obtained by a number of other methods (see [17] and results in previous sections). If we treat the penalty term semi-implicitly as in (2.8) or (3.3) then we achieve the same evolution speed but the stiffness matrix would depend on time and we have to solve a linear system in obtaining $\mathbf{d}$ at every time step, which can be very costly when a fine mesh is used since we prefer to use a direct linear system solver. In this section, we propose a fixed point iterative method to treat the penalty term in (3.3) while keeping the other part unchanged. Then the stiffness matrix at each time step and each fixed point iteration will remain the same. That is, we solve (3.3) by the following iterative algorithm with $s = 1, 2, \ldots$

$$\int_\Omega \left(\frac{\bar{\mathbf{d}}_s - \mathbf{d}_h^n(\mathbf{X}^n)}{\Delta t} \cdot \mathbf{e} + \gamma \nabla \bar{\mathbf{d}}_s : \nabla \mathbf{e} + \frac{\gamma}{\epsilon^2} \left(|\mathbf{d}_h^n|^2 - 1 \right) \bar{\mathbf{d}}_{s-1} \cdot \mathbf{e} \right) \mathrm{d}\mathbf{x} = 0, \tag{4.4}$$

where we choose $\bar{\mathbf{d}}_0 = \mathbf{d}_h^n$. Obviously, the stiffness matrix of (4.4) is independent of time and the fixed point iteration. This will largely reduce the computational time of a direct linear system solver to obtain an evolution solution over a time interval.

An L_2 convergence of the iterative method can be easily obtained for our typically chosen ϵ, γ and Δt in previous sections. Subtracting (4.4) from (3.3) we have

$$\int_\Omega \left[\left(\mathbf{d}_h^{n+1} - \bar{\mathbf{d}}_s \right) \cdot \mathbf{e} + \gamma \Delta t \nabla \left(\mathbf{d}_h^{n+1} - \bar{\mathbf{d}}_s \right) : \nabla \mathbf{e} \right] \mathrm{d}\mathbf{x} = -\frac{\gamma \Delta t}{\epsilon^2} \int_\Omega \left[\left(|\mathbf{d}_h^n|^2 - 1 \right) \left(\mathbf{d}_h^{n+1} - \bar{\mathbf{d}}_{s-1} \right) \cdot \mathbf{e} \right] \mathrm{d}\mathbf{x}. \tag{4.5}$$

Taking $e = \mathbf{d}_h^{n+1} - \bar{\mathbf{d}}_s$ and using Cauchy–Schwarz inequality we obtain

$$\|\mathbf{d}_h^{n+1} - \bar{\mathbf{d}}_s\|^2 + \Delta t \|\nabla (\mathbf{d}_h^{n+1} - \bar{\mathbf{d}}_s)\|^2 \leqslant \frac{\gamma \Delta t}{\epsilon^2} \|\mathbf{d}_h^{n+1} - \bar{\mathbf{d}}_{s-1}\| \|\mathbf{d}_h^{n+1} - \bar{\mathbf{d}}_s\|.$$

We thus have

$$\|\mathbf{d}_h^{n+1} - \bar{\mathbf{d}}_s\| \leqslant \frac{\gamma \Delta t}{\epsilon^2} \|\mathbf{d}_h^{n+1} - \bar{\mathbf{d}}_{s-1}\|. \tag{4.6}$$

So the fixed point iterative method converges in the sense of L_2 norm if $\frac{\gamma \Delta t}{\epsilon^2} < 1$. This condition implies that the iterative method will be acceptable and useful for moderately small ϵ since relatively large Δt may still be used. As we mentioned earlier when ϵ is extremely small the model itself would be difficult to be numerically solved since the energy may be too large to be represented accurately. In any case, the condition is satisfied by our test cases and typical choice of parameters in previous sections. However, when we apply the iterative method (4.4)

to Example 2.2 with zero initial velocity under a 16×16 grid and same parameters the result with five fixed point iterations does not perfectly match with that of (3.3) as depicted in Fig. 6.

We can observe some difference between two solutions. Such a difference can also be seen from the energy calculation. At $t = 0.25$ with the 16×16 grid $E = 13.750$ if using the scheme (3.3) whereas $E = 15.058$ if using the iterative scheme (4.4). We increase the number of iterations to 15 and see no improvement. The reason is that the solution $\mathbf{d}_h^{n+1}$ of (3.3) and the solution $\bar{\mathbf{d}}_s$ of (4.4) are both in $\mathbf{H}^1$, but our iterative convergence is showed only in the sense of L_2 norm. So the approximation $\nabla \bar{\mathbf{d}}_s$ to $\nabla \mathbf{d}_h^{n+1}$ in the variational form (3.3) would not be completely guaranteed by the L_2 convergence. Nevertheless, if the mesh is fine enough (especially refined near the defect points) we expect that a good approximation may still be achieved. Hence, we test a 64×64 grid and the energies with five fixed point iterations near annihilation are given in the following table.

Energies computed	$t = 0.25$	$t = 0.26$
Scheme (3.3)	14.1312	12.559
Scheme (4.4)	14.1306	12.557

We see that under the fine grid the evolution of the solution using the fixed point iterative method (4.4) matches very well with the scheme (3.3). From such a fine grid calculation it seems to us that the annihilation time is actually close to $t = 0.26$. Velocities near annihilation obtained from schemes (3.3) and (4.4) are depicted in Fig. 7 and we observe no obvious difference.

In summary, the philosophy of our choice of algorithms to compute this liquid crystal flow model is: when a coarse grid is good enough to do the computation the computational time of schemes (3.3) and (4.4) has no significant difference, then scheme (3.3) is recommended; when we need to use a very fine grid to do the computation then the computational time of scheme (4.4) would be significantly less than scheme (3.3) and at the same time the evolution of the solution under a very fine grid would be expected to match well with that of scheme (3.3) for moderate size of ϵ. Thus, scheme (4.4) is recommended.

Next, we will use the faster splitting C^0 finite element algorithm to compute a few more cases with different domain geometries and parameters.

5. More numerical experiments

5.1. The distance of two defect points versus time

From the momentum equation (1.1) we see that the parameter λ reflects the effect of the director field to the flow field. In Example 2.2 with zero initial field, if λ is smaller the effect of director field to the flow field

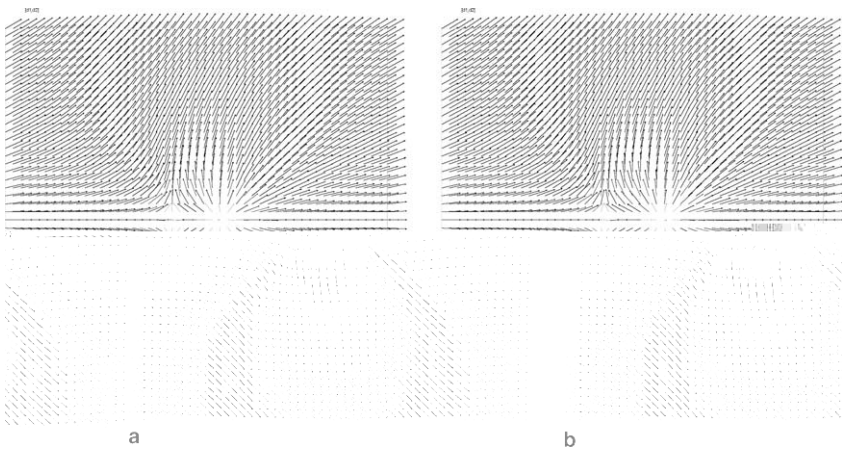

Fig. 6. Director fields of Example 2.2 with zero initial velocity on a 16×16 grid: (a) scheme (3.3) at $t = 0.25$; (b) scheme (4.4) at $t = 0.25$.

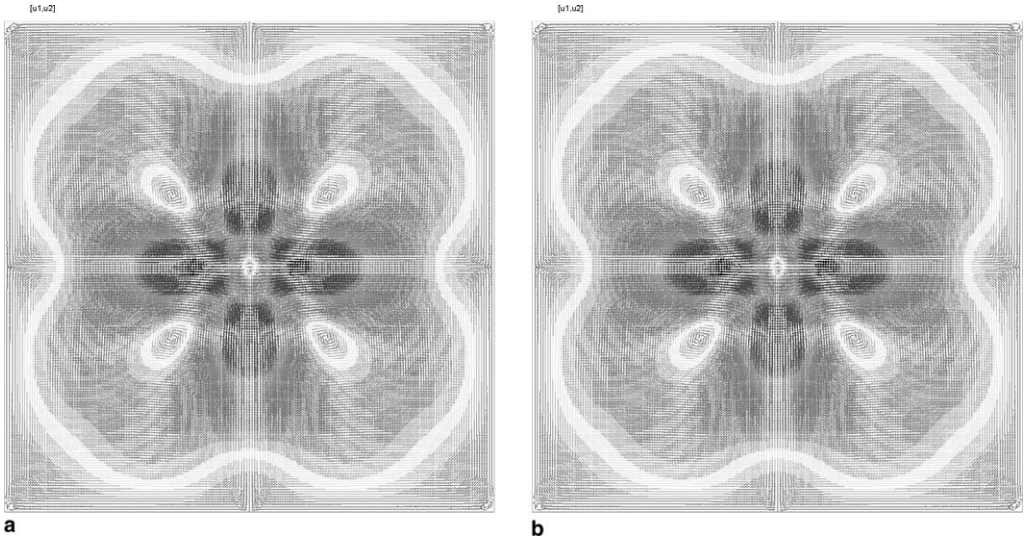

Fig. 7. Velocity fields of Example 2.2 at $t = 0.26$ on a 64×64 grid: (a) scheme (3.3); (b) scheme (4.4).

would be smaller and the flow velocity would be smaller. Hence, from the Eq. (1.3) the director field would transport slower and thus two defect points would move slower. So, intuitively speaking, we expect that when λ is small the motion of defects towards the origin in Example 2.2 would be slower than when λ is large since the director field disturbs the flow field less. Below we compute Example 2.2 using the scheme (3.3) on a 16×16 grid with three different values of $\lambda = 0.1$, 1, and 10 (and the other parameters are the same as before) (see Fig. 8).

The results verify our expectation. On the other hand, from the energy law (2.5), we can see that with larger λ, the overall system will approach the equilibrium faster than the case with smaller λ, hence, resulting in the defect points moving faster. This again confirms the fact that the induced elastic stress is a system stabilization factor.

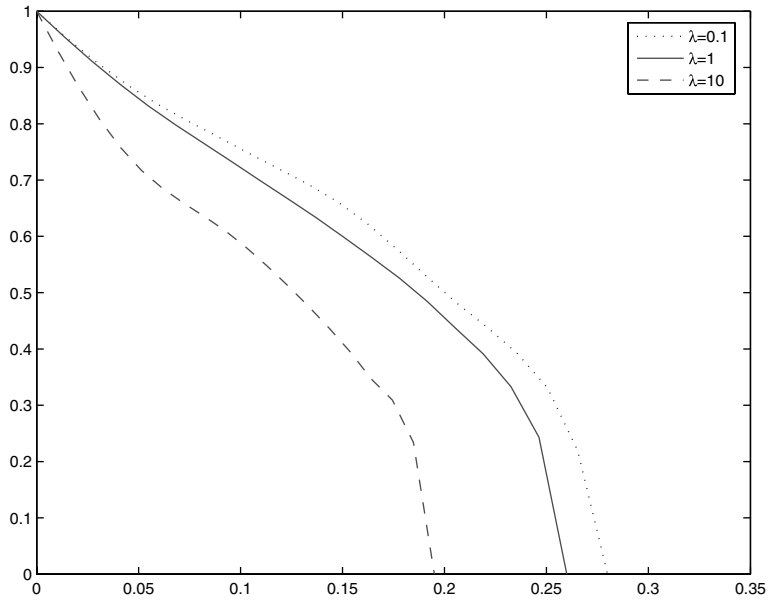

Fig. 8. Time–distance relation with a few different λ.

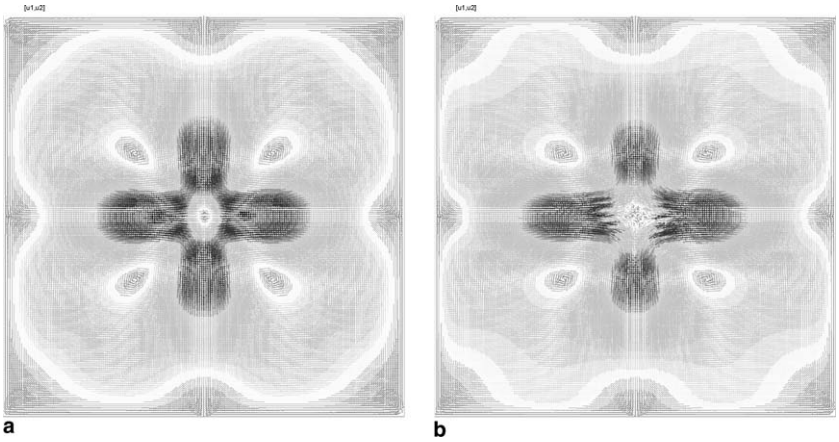

Fig. 9. Velocity fields **u** near the annihilation for various Reynolds numbers: (a) $\nu = 1/10$ at $t = 0.24$; (b) $\nu = 1/100$ at $t = 0.23$.

5.2. Effects of various Reynolds numbers or viscosities

We now give computational results for Example 2.2 with various Reynolds numbers. To see details of velocity fields with higher Reynolds numbers we would use a 64×64 grid and the scheme (4.4) with five fixed point iterations. We have shown the velocity field with $\nu = 1$ at the annihilation time $t = 0.26$ in Fig. 7. For $\nu = 1/10$ and $1/100$ velocity fields near the annihilation are depicted in Fig. 9.

It seems that a more refined mesh in the middle part of the domain may be needed for the $\nu = 1/1000$ case. We consider a mesh which is finer in the middle part of the domain and coarser near the boundary. The velocity field for $\nu = 1/1000$ is shown in Fig. 10.

The results look like being opposite to the energy dissipation law since when Reynolds number increases or the viscosity decreases it seems that the energy may dissipate slower (see the right-hand side of (2.5)) and that the system may possibly reach the equilibrium state later. We might then think that the annihilation occurs later as well. Numerical experiments above indicate that this is not the case. When the viscosity decreases the annihilation actually occurs sooner. There is certainly no contradiction here since the annihilation is not the equilibrium state and the energy dissipation rate does not necessarily monotonically depend on ν since the change of ν also makes changes in **u** and **d** which appear in the right-hand side of (2.5) and influence the dissipation rate as well. The situation here is just more complicated and subtle and cannot be explained simply from the energy law. We think that the annihilation time is mainly determined by the flow field or the traveling

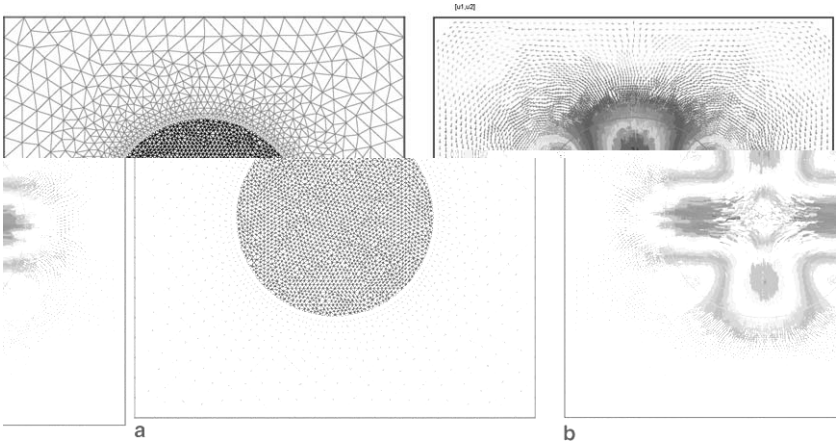

Fig. 10. Mesh and the velocity field for $\nu = 1/1000$: (a) Mesh refined in the middle domain; (b) $\nu = 1/1000$ at $t = 0.225$.

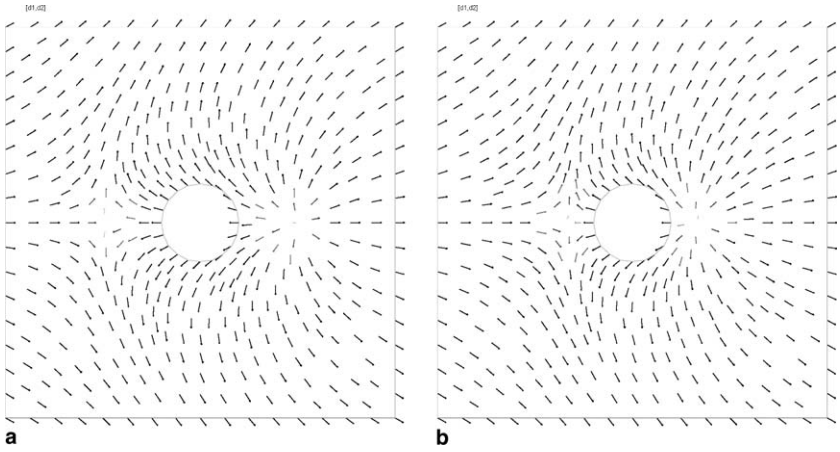

Fig. 11. Director fields **d** in a square domain with a circular hole: (a) $t = 0$; (b) $t = 0.2$.

velocity of the liquid crystal molecules. When Reynolds number increases or the viscosity decreases the flow field is dissipated less (expected from the momentum equation (1.1)). Hence, the liquid crystal molecules (and then the defect points) move faster and the annihilation occurs sooner. When the viscosity increases the flow field is dissipated more and the defect points move slower. Consequently, the annihilation occurs later.

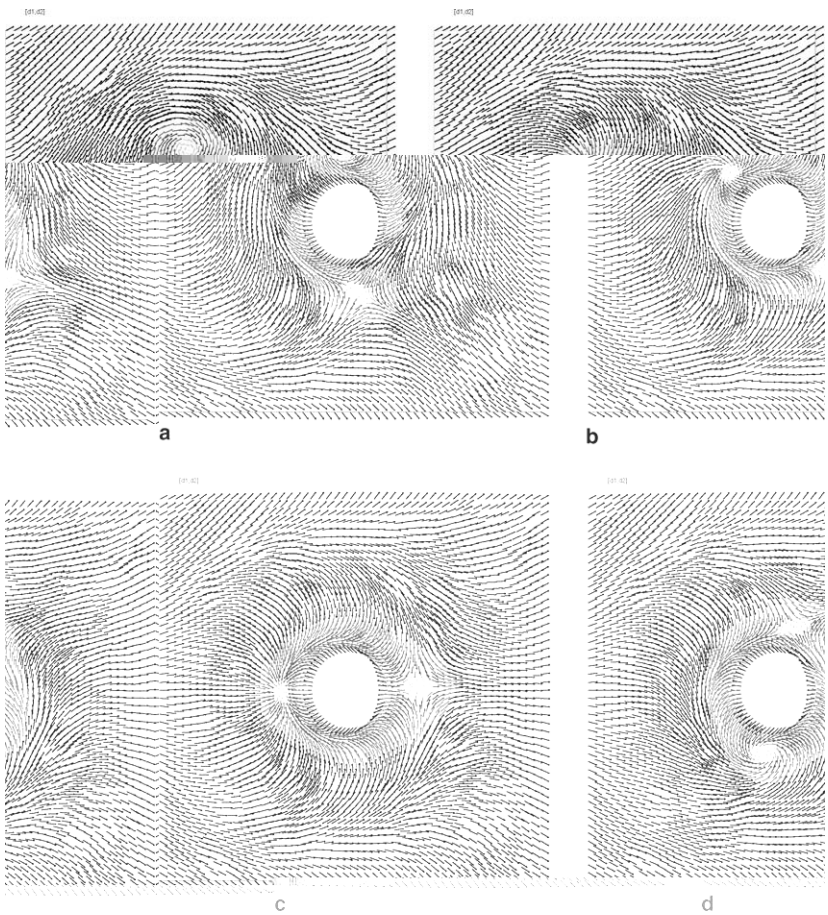

Fig. 12. Director fields with a rotational initial flow field for domain with a hole: (a) $t = 0.10$; (b) $t = 0.15$; (c) $t = 0.20$; (d) $t = 0.25$.

On the other hand, when the viscosity decreases we do observe that the system reaches the equilibrium state later as we expected above although the annihilation occurs sooner. We conduct a numerical test for $v = 1$ and $v = 1/10$ case and denote E_1 as the energy for $v = 1$ and $E_{0.1}$ as the energy for $v = 1/10$. After the annihilation, say, at $t = 0.3$, $E_1 \approx 2.7$ and $E_{0.1} \approx 2.5$. Later, the dissipation E_1 becomes faster than that of $E_{0.1}$. At $t = 0.35$ we have $E_1 \approx 1.7$ whereas $E_{0.1} \approx 1.9$, and at $t = 0.4$ we have $E_1 \approx 1.4$, whereas $E_{0.1} \approx 1.6$. Eventually, the system with $v = 1$ will reaches the equilibrium sooner than that with $v = 0.1$.

5.3. A square domain with a hole

We see that in Example 2.2 two defect points move towards the middle of the domain if the initial velocity field is zero. It is curious where these defect points would move if there is a hole in the middle of the domain. We use the scheme (3.3) and a roughly 16×16 grid with the same parameters used Section 2 to compute the solution. We observe that the defect points move towards the middle of the domain. However, they eventually stop near the boundary of the circular hole (see Fig. 11).

If we have a rotational flow field at the beginning in a square domain without a hole the result in Section 2 showed that the two defect points would merge (annihilate) around the origin around $t = 0.2$. Here, we compute the solution again for the square domain with a hole centered at the origin. The result is depicted in Fig. 12.

We observe that two defect points move towards the boundary of the circular hole and at the same time rotate around the hole at around the same speed as the initial velocity field (approximately three revolutions per unit time). It seems that unlike the case without a hole these two defect points would not merge.

Acknowledgments

P. Lin is partially supported by Singapore Academic Research Grant No. R-146-000-033-112. C. Liu is partially supported by NSF Grant DMS-0405850. This work has begun when C. Liu was visiting the National University of Singapore in the winter of 2004. He wants to thank the hospitality and the assistance provided by the Department of Mathematics and Institute for Mathematical Sciences in NUS. P. Lin wants to thank Olivier Pironneau for his help with Freefem++ and for his valuable discussion on the algorithm.

References

[1] P. Aviles, Y. Giga, A mathematical problem related to the physical theory of liquid crystal configurations, Proc. Centre Math. Anal. Austral. Nat. Univ. 12 (1987) 1–16.
[2] F. Brezzi, M. Fortin, Mixed and Hybrid Finite Element Methods, Springer, Berlin, 1991.
[3] R. Cohen, S.-Y. Lin, M. Luskin, Relaxation and gradient methods for molecular orientation in liquid crystals, Comput. Phys. Commun. 53 (1989) 455–465.
[4] R. Cohen, R. Hardt, D. Kinderlehrer, S.-Y. Lin, M. Luskin, in: J.L. Ericksen, D. Kinderlehrer (Eds.), Theory and Applications of Liquid Crystals, IMA Volumes in Mathematics and its Applications, vol. 5, Springer, Berlin, 1987.
[5] Peter J. Collings, Liquid Crystals, Nature's Delicate Phase of Matter, Princeton University Press, Princeton, NJ, 2001.
[6] J. Douglas, T.F. Russell, Numerical methods for convection dominated diffusion problems based on combining the method of characteristics with finite element methods or finite difference method, SIAM J. Numer. Anal. 19 (1982) 871–885.
[7] Qiang Du, Benyu Guo, Jie Shen, Fourier spectral approximation to a dissipative system modeling the flow of liquid crystals, SIAM J. Numer. Anal. 39(3) 735–762.
[8] P.G. de Gennes, J. Prost, The Physics of Liquid Crystals, second ed., Oxford Science Publications, Oxford, 1993.
[9] V. Girault, P.-A. Raviart, Finite Element Methods for Navier–Stokes Equations, Theory and Algorithms, Springer, Berlin, 1986.
[10] R. Glowinski, P. Lin, X. Pan, An operator-splitting method for a liquid crystal model, Comput. Phys. Commun. 152 (2003) 242–252.
[11] R. Glowinski, P. Le Tallec, Augmented Lagrangian and Operator-Splitting Methods in Nonlinear Mechanics, SIAM (1989).
[12] R. Hardt, D. Kinderlehrer, Mathematical questions of liquid crystal theory, in: J.L. Ericksen, D. Kinderlehrer (Eds.), Theory and Applications of Liquid Crystals, IMA Volumes in Mathematics and its Applications, vol. 5, Springer, Berlin, 1987, pp. 151–184.
[13] F.H. Lin, Nonlinear theory of defects in nematic liquid crystals, phase transitions and flow phenomena, Commun. Pure Appl. Math. 42 (1989) 789–814.
[14] F.H. Lin, C. Liu, Nonparabolic dissipative systems, modeling the flow of liquid crystals, Commun. Pure Appl. Math. 48 (1995) 501–537.
[15] Ping Lin, A sequential regularization method for time-dependent incompressible Navier–Stokes equations, SIAM J. Numer. Anal. 34 (1997) 1051–1071.

[16] P. Lin, X. Chen, M.T. Ong, Finite element methods based on a new formulation for the non-stationary incompressible Navier–Stokes equations, Int. J. Numer. Method Fluids 46 (2004) 1169–1180.
[17] C. Liu, N.J. Walkington, Approximation of liquid crystal flows, SIAM J. Numer. Anal. 37 (3) (2000) 725–741.
[18] C. Liu, N.J. Walkington, Mixed methods for the approximation of liquid crystal flows, M2AN 36 (2) (2002) 205–222.
[19] O. Pironneau, On the transport-diffusion algorithm and its applications to the Navier–Stokes equations, Numer. Math. 38 (1982) 309.
[20] H. Rui, M. Tabata, A second order characteristic finite element scheme for convection diffusion problems, Numer. Math. 92 (2002) 161–177.